ACS Catalysis

Research Article

pubs.acs.org/acscatalysis

Site-Isolated Molecular Iridium Complex Catalyst Supported in the 1-Dimensional Channels of Zeolite HSSZ-53: Characterization by Spectroscopy and Aberration-Corrected Scanning Transmission Electron Microscopy

Jing Lu,[†] Ceren Aydin,[†] Ann J. Liang,[§] Cong-Yan Chen,[§] Nigel D. Browning,[†,‡,∥] and Bruce C. Gates*[,†]

[†]Department of Chemical Engineering and Materials Science and [‡]Department of Molecular and Cellular Biology, University of California, One Shields Avenue, Davis, California 95616, United States

[§]Chevron Energy Technology Company, 100 Chevron Way, Richmond, California 94802, United States

Supporting Information

ABSTRACT: Zeolite HSSZ-53, which has 1-dimensional channels with 14-ring extra-large pores, was used as a support for a molecular iridium complex synthesized from $Ir(C_2H_4)_2(C_5H_7O_2)$ and characterized with infrared (IR) and extended X-ray absorption fine structure (EXAFS) spectroscopies and atomic-resolution aberration-corrected scanning transmission electron microscopy (STEM). The spectra show that $Ir(C_2H_4)_2(C_5H_7O_2)$ reacted readily with the bridging OH groups of the zeolite, leading to the removal of $C_5H_7O_2$ ligands and the formation of mononuclear $Ir(C_2H_4)_2$ complexes bonded to the zeolite by Ir−O bonds at the framework aluminum sites. STEM images confirm the spectra, showing site-isolated iridium centers within the zeolite channels, with no evidence of iridium clusters. The samples constitute a highly uniform, well-defined array of essentially molecular catalytic species in a highly uniform, confined environment, allowing precise investigations of the chemistry of the iridium complex in the absence of solvents. IR spectra show that the supported $Ir(C_2H_4)_2$ complexes were converted to $Ir(C_2H_5)_2$, $Ir(CO)_2$, $Ir(CO)(C_2H_4)$, and $Ir(CO)(C_2H_4)_2$ as various mixtures of H_2, CO, and C_2H_4 reacted with the sample. The sample was tested as a catalyst for ethylene hydrogenation and for H−D exchange in the reaction of $H_2 + D_2$. The data, combined with results reported for isostructural iridium complexes bonded to zeolite HY and to MgO, demonstrate how the catalytic activity can be tuned by choice of the support, with the support being characterized as a ligand with electron-donating or electron-withdrawing properties. The results demonstrate that the rate of ethylene hydrogenation catalyzed by the supported iridium complexes is limited by H_2 activation when the iridium is electron rich (on the MgO support), whereas the rate-limiting step is C_2H_4 adsorption when the iridium is electron deficient (on either zeolite support).

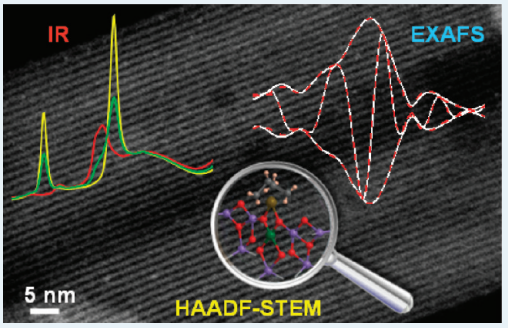

KEYWORDS: *supported iridium complex catalyst, zeolite HSSZ-53, IR spectroscopy, EXAFS spectroscopy, aberration-corrected STEM, ethylene hydrogenation, H−D exchange, support effect*

INTRODUCTION

Some of the most efficient solid catalysts consist of essentially molecular or nanostructured metal-containing species dispersed on supports, because they combine the advantages of high surface area, minimal corrosion, and ease of separation from products.[1−3] Characterization of the structures and reactivities of such catalysts is often hindered by the smallness and nonuniformity of the supported structures, and the nonuniformity of the support often contributes to this nonuniformity, especially when the supported species are so small that they are essentially molecular and the support, as a ligand, contributes significantly to the activity.[4,5] Thus, when a research goal is to determine the chemistry of supported molecular catalysts, the best supports are often those with highly uniform structures, and zeolites (crystalline aluminosilicates) are among the most widely investigated supports in this class.[6−8]

Here, we report results characterizing the synthesis, structure, reactivity, and catalytic properties of essentially molecular iridium complexes bonded within the highly crystalline zeolite HSSZ-53 in the aluminosilicate form.[9] The framework of HSSZ-53 consists of one-dimensional, nonintersecting channels which have 14-ring extra-large pores with dimensions of 6.4 × 8.7 Å (Figure 1) to facilitate ingress of the molecular precursor $(Ir(C_2H_4)_2(acac))$ (acac is acetylacetonate) used to prepare the supported iridium complex. We chose this zeolite because it offers the opportunity for preparation of highly uniform supported catalysts synthesized by stoichiometrically simple reactions. Such catalysts lend themselves to precise structure

Received: February 26, 2012
Revised: April 12, 2012
Published: April 18, 2012

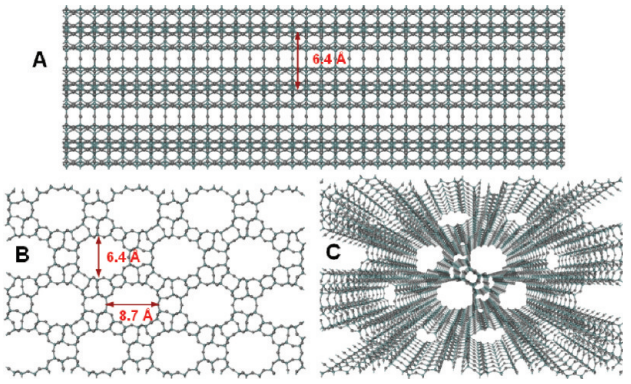

Figure 1. Models of zeolite HSSZ-53 framework constructed from crystallographic data: views from the [010] (A) and [100] (B) projections, and perspective view from the [100] projection (C). The double-headed arrows indicate the diameters of a HSSZ-53 channel in each projection.

determinations by spectroscopy combined with atomic-resolution microscopy, and our intent was that the catalyst be among the best-defined solid catalysts.

RESULTS

Characterization of Initially Prepared Catalyst by Infrared Spectroscopy: Formation of $Ir(C_2H_4)_2$ Complexes on the Acidic Sites of Zeolite HSSZ-53. The supported catalyst was synthesized by the reaction of $Ir(C_2H_4)_2(acac)$ slurried in *n*-pentane with zeolite HSSZ-53 powder. During the synthesis, the color of the solution changed from orange-yellow to colorless, indicating the nearly complete uptake of the precursor by the support. The solvent was removed by evacuation, and the preparation conditions were chosen to give an iridium loading of 1 wt %.

Infrared (IR) spectra in the ν_{OH} and 1300−1700 cm^{-1} regions characterizing the zeolite before and after the reaction with $Ir(C_2H_4)_2(acac)$ are shown in Figure 2. The spectrum of the bare zeolite in the ν_{OH} region includes bands at 3739 (assigned to the terminal silanol groups of the zeolite) and 3632 cm^{-1} (assigned to the acidic hydroxyl groups[10]). The intensity of the 3632 cm^{-1} peak decreased significantly after the reaction of $Ir(C_2H_4)_2(acac)$ with the zeolite, but the intensity of the 3739 cm^{-1} peak remained essentially unchanged, indicating that the precursor had reacted preferentially with the Al−O^- sites. In the 1300−1700 cm^{-1} region (Figure 2B), the spectrum of the sample incorporating the supported iridium complex includes new bands at 1366, 1537, and 1598 cm^{-1}. These bands are assigned to δ_{CH}, ν_{C-C-Cs}, and ν_{COring}, respectively, resembling those characterizing Hacac adsorbed on the zeolite.[11,12] Thus, the IR data indicate that acac ligands were dissociated from the iridium as a result of the reaction of the precursor with the acidic OH groups of the zeolite, forming chemisorbed iridium complexes.

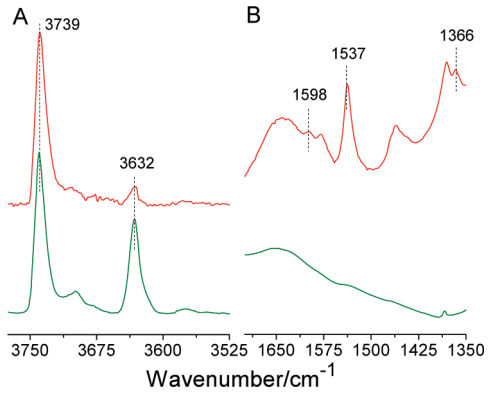

Figure 2. IR spectra (absorbance) in the ν_{OH} (A) and 1300−1700-cm^{-1} regions (B) characterizing the following samples: HSSZ-53 zeolite after calcination (bottom) and sample formed by reaction of the zeolite with $Ir(C_2H_4)_2(acac)$ after removal of the *n*-pentane solvent (top).

The IR spectra of this supported sample demonstrate the presence of ethylene ligands bonded to the iridium (Figure 3a),

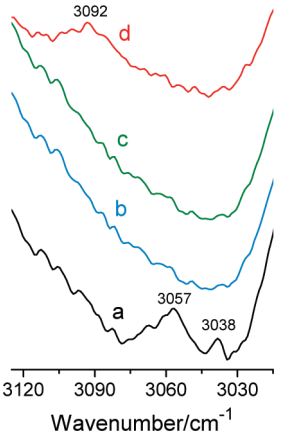

Figure 3. IR spectra (absorbance) in the ν_{CH} region characterizing the sample formed by adsorption of $Ir(C_2H_4)_2(acac)$ on zeolite HSSZ-53 as it was treated in flowing gases at 298 K and atmospheric pressure, as follows: (a) helium, (b) a pulse of CO in helium, (c) H_2 + C_2H_4 for 10 min (recorded after purging of the gas-phase C_2H_4 from the cell with helium), and (d) a pulse of CO in helium, followed by C_2H_4 for 15 min (after purging of gas-phase C_2H_4 from the cell with helium).

indicated by the bands at 3038 and 3057 cm^{-1} (assigned to ν_{CH} bands of π-bonded ethylene),[13−15] which nearly match those of the precursor $Ir(C_2H_4)_2(acac)$.[16] This observation indicates that the ethylene ligands remained bonded to the iridium during the chemisorption.

Characterization of the Supported Iridium Complex by EXAFS and XANES Spectroscopies. Further evidence of the structure of the supported iridium species is provided by extended X-ray absorption fine structure (EXAFS) spectra measured at the Ir L_{III} edge. Results are shown in Figure 4, which includes k^1- and k^3-weighted EXAFS data (k is the wave vector) and Fourier transformed data, along with the best fits of the data. The structural parameters obtained by fitting the data to three candidate models are shown in Table 1 and Supporting Information Table S1. Assessments of the candidate models and explanations of why all but one were rejected are summarized in Supporting Information Table S2.

As shown in Table 1, the model that gives the best fit of the data indicates iridium bonded to two ethylene ligands and to two oxygen atoms of the support. The evidence of the ethylene ligands, including an Ir−C coordination number of nearly 4, is consistent with the IR spectra. The Ir−O distance (2.10 Å) is a typical distance for bonding of group-9 metal complexes to oxygen atoms on the surfaces of metal oxides and zeolites.[17,18]

Thus, the EXAFS results bolster the IR data, demonstrating the presence of $Ir(C_2H_4)_2$ complexes bonded to the zeolite and

dx.doi.org/10.1021/cs300139p | ACS Catal. 2012, 2, 1002−1012

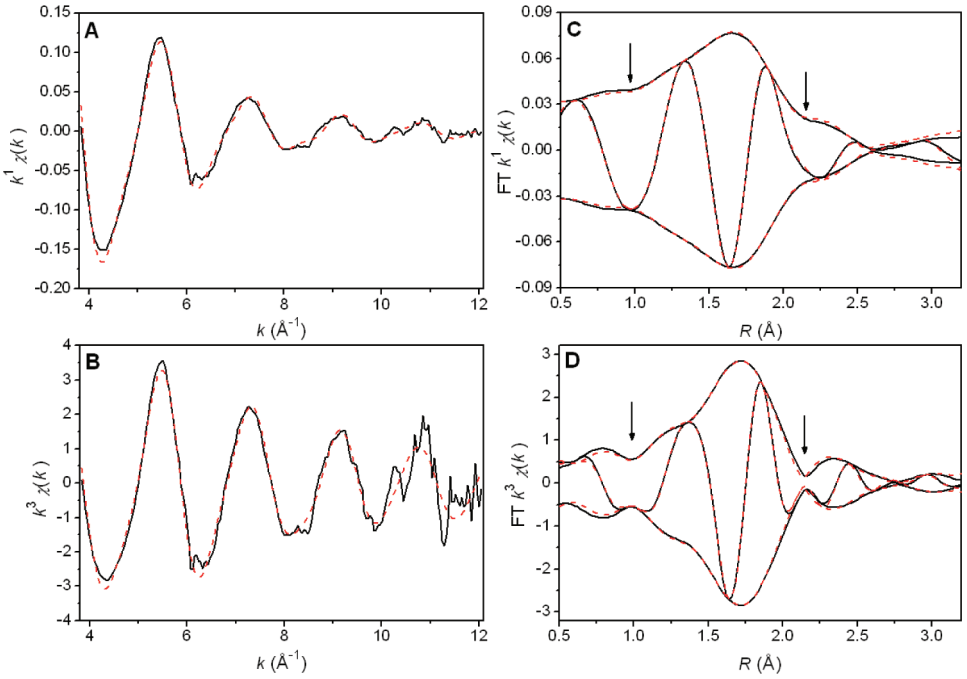

Figure 4. Results of EXAFS analysis characterizing the sample formed by the reaction of $Ir(C_2H_4)_2(acac)$ with zeolite HSSZ-53. k^1-Weighted (A) and k^3-weighted (B) EXAFS function (solid line) and sum of calculated contributions (dashed line) determined for the best fit model (Model I). k^1-weighted (C) and k^3-weighted (D) imaginary part and magnitude of the Fourier transform of the data (solid line) and sum of the calculated contributions determined for the best fit model (Model I in Supporting Information Table S1). The arrows in C and D indicate a constructive/destructive feature attributed to the presence of the various shells.

Table 1. EXAFS Parameters Determined for the Best Fit Model Characterizing the Sample Formed by the Reaction of $Ir(C_2H_4)_2(acac)$ with HSSZ-53[a]

absorber–backscatterer pair	N	R (Å)	$10^3 \times \Delta\sigma^2$ (Å^2)	ΔE_0 (eV)	goodness of fit
Ir–$O_{zeolite}$	2.1	2.10	2.4	−4.1	5.7
Ir–C	3.9	2.01	7.1	0.38	
Ir–Al	1.0	2.89	9.6	−0.50	

[a]Fit details: Range of data used in fitting: 0.5 < R < 3.2 Å, 3.84 < k < 12.06 Å^{-1}. Error in EXAFS function: 0.0006. Notation: N, coordination number; R, distance between absorber and backscatterer atoms; $\Delta\sigma^2$, disorder term relative to the reference; ΔE_0, inner potential correction relative to the reference. Error bounds (accuracies) of the structural parameters are estimated to be as follows: N, ±20%; R, ±0.02 Å; $\Delta\sigma^2$, ±20%; and ΔE_0, ±20%.

resulting from the dissociation of the acac ligands and the formation of two Ir–$O_{zeolite}$ bonds replacing the Ir–O_{acac} bonds in the precursor $Ir(C_2H_4)_2(acac)$. Consistent with this conclusion, the EXAFS data give evidence of an Ir–Al contribution with a coordination number of nearly 1 at a distance of 2.89 Å, confirming the IR data (Figure 2A) and showing that the iridium complex was bonded at Al sites where acidic OH groups had been removed by the chemisorption.

The iridium in the supported complex has a formal oxidation state of +1, and the complex is coordinatively unsaturated, formally being a 16e$^-$ species (8e$^-$ from Ir$^+$, 4e$^-$ from AlO_2^- of the zeolite, and 4e$^-$ from the two ethylene ligands). XANES spectra (Supporting Information Figure S4) show that the edge position of the freshly prepared sample is approximately 2 eV higher in energy than that of bulk iridium metal. Moreover, the white line intensity of the supported iridium complex is significantly greater than that of supported Ir_4 clusters[19] and of bulk iridium metal. These comparisons confirm the presence of cationic iridium and weigh against a detectable amount of iridium clusters and particles incorporating zerovalent iridium in the sample.

Consistent with this inference, there was no EXAFS evidence of Ir–Ir contributions; attempts to include such a contribution in the data fitting led to unsatisfactory fits (Table 1 and Supporting Information Tables S1 and S2; details of the fitting are shown in Supporting Information). The lack of a detectable Ir–Ir contribution indicates the absence of iridium clusters and consequently the presence of only isolated mononuclear iridium complexes in the sample. The possibility that small amounts of iridium clusters or particles too small to detect by EXAFS or XANES spectroscopy (roughly a few percent of the total iridium) is ruled out by the images determined by electron microscopy, as summarized below.

The IR and EXAFS data essentially match results[20] showing how $Ir(C_2H_4)_2(acac)$ reacts with dealuminated HY zeolite. We infer that the synthesis may be quite general for acidic zeolites reacting with $Ir(C_2H_4)_2(acac)$. The synthesis route is even more general: similar chemistry has been observed for $Rh(C_2H_4)_2(acac)$ and $Ru(C_2H_4)_2(acac)_2$.[21,22]

In summary, the spectroscopic data indicate the structure of the supported iridium complex represented in Scheme 1.

Aberration-Corrected HAADF-STEM Evidence of Site-isolated Iridium Complexes in the Zeolite. Figure 5A shows aberration-corrected STEM images of the sample prepared by the reaction of $Ir(C_2H_4)_2(acac)$ with the zeolite. The images were recorded in the high-angle annular dark-field (HAADF) mode, so that the intensity of the dominant scattering mechanism that gives rise to the contrast is roughly proportional to the square of the atomic number (Z^2) of the element.[23] Thus, single Ir atoms (Z = 77) appear as bright scattering centers (Figure 5) in the zeolite structure, which

dx.doi.org/10.1021/cs300139p | ACS Catal. 2012, 2, 1002–1012

Scheme 1. Structural Model of Zeolite HSSZ-53-Supported Iridium Complex (Distances in Å Determined by EXAFS Spectroscopy)

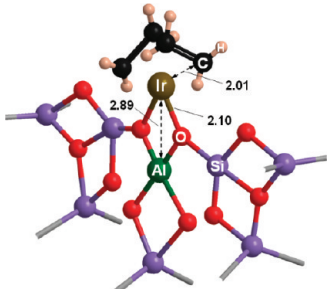

consists of only light atoms: Si (Z = 14), Al (Z = 13), O (Z = 8) and H (Z = 1). The images of Figure 5 show that single Ir atoms were isolated and well dispersed within the channels of the zeolite. These images, and others recorded at lower magnification (Figure 6), give no evidence of iridium clusters, consistently indicating that the mononuclear iridium complexes identified by IR and EXAFS spectra were isolated in the zeolite channels and the only iridium species present in them.

Additional images of the same area shown in Figure 5A were recorded after prolonged exposure (30 s) of the sample to the electron beam. The images show that exposure of the sample to the beam caused both damage to the zeolite framework[24,25] and movement of Ir atoms,[26] leading to the formation of iridium clusters. As shown in Figure 7, after 30 s of beam exposure, significant damage to the zeolite framework had occurred. Aggregation of the Ir atoms to form clusters occurred only in the regions where the zeolite framework had been destroyed. These results indicate that movement of the Ir atoms caused by the electron beam was limited by the confinement to intact zeolite channels,[27] consistent with our inference that the iridium complexes in the initially prepared sample were bonded within these channels.

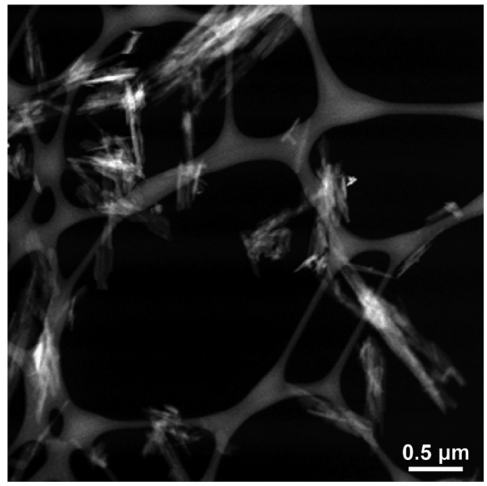

Figure 6. Low-magnification HAADF-STEM image characterizing the sample prepared by the reaction of $Ir(C_2H_4)_2(acac)$ with zeolite HSSZ-53. The image shows the needle-shaped crystals of the zeolite and is consistent with the absence of iridium clusters.

Reaction of Iridium Diethylene Complexes with CO: Evidence of High Degree of Uniformity of the Supported Complexes. The zeolite-supported iridium diethylene complexes were probed with CO to form iridium dicarbonyls, because the IR spectra of these species provide evidence of the uniformity of the supported complexes. When a 20-mL pulse of CO in flowing helium was brought in contact with the supported iridium diethylene complex, CO ligands rapidly displaced the C_2H_4 ligands, as shown by the disappearance of the IR bands at 3038 and 3057 cm^{-1} (Figure 3b) and the concomitant growth of new bands at 2027 and 2099 cm^{-1} (Figure 8a and 8b), assigned to iridium *gem*-dicarbonyls.[28−30] The sharp new bands, each with a full width at half-maximum of only about 10 cm^{-1}, indicate that the iridium species had a high degree of uniformity.[31] Furthermore, the absence of CO bands other than those characterizing the

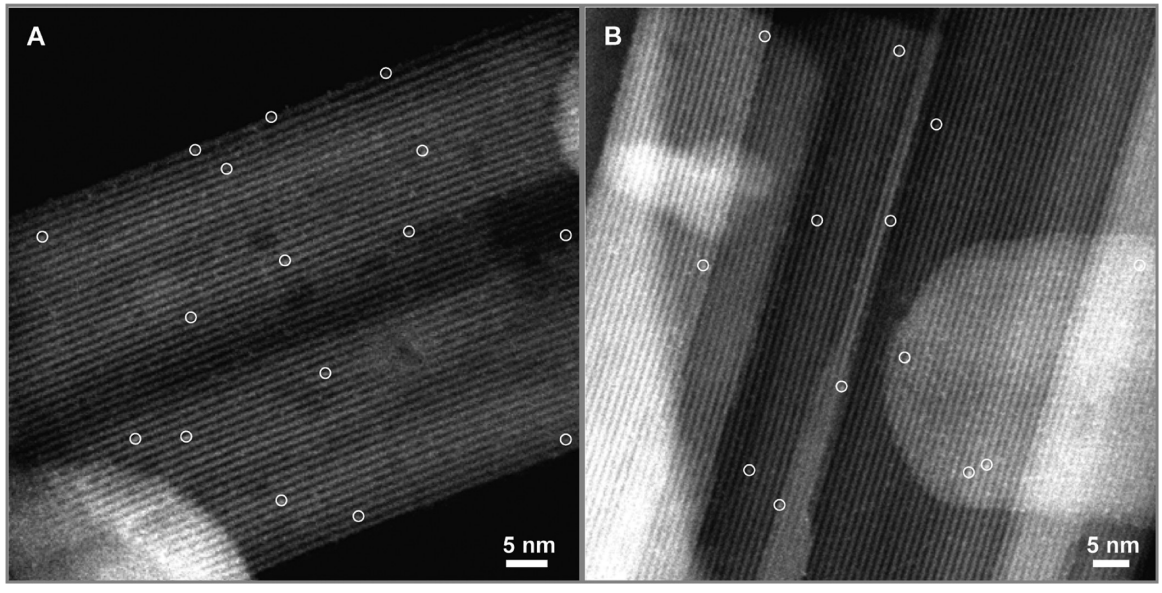

Figure 5. HAADF-STEM (Z-contrast) images characterizing the catalyst prepared by the reaction of $Ir(C_2H_4)_2(acac)$ with zeolite HSSZ-53: (A) the initially prepared catalyst and (B) the catalyst after it had been used for ethylene hydrogenation. The images show individual Ir atoms (some of them indicated by white circles) well dispersed inside the 1-D channels of the zeolite and in the absence of detectable iridium clusters.

dx.doi.org/10.1021/cs300139p | *ACS Catal.* 2012, 2, 1002−1012

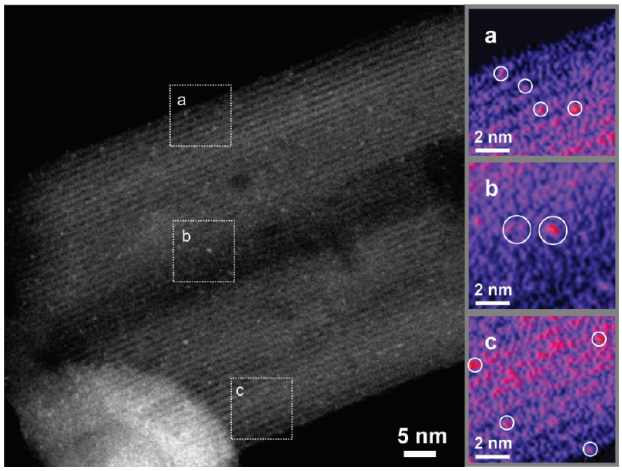

Figure 7. HAADF-STEM (*Z*-contrast) image characterizing the catalyst prepared by the reaction of $Ir(C_2H_4)_2(acac)$ with zeolite HSSZ-53. The image is of the same region shown in Figure 5A after exposure of the sample to the electron beam for 30 s. The image shows the deterioration of the zeolite framework as a result of the irradiation and give evidence of small iridium clusters in some regions, the formation of which is inferred to have been caused by the electron beam. Colored views of the boxed region (a–c) in the image are shown on the right.

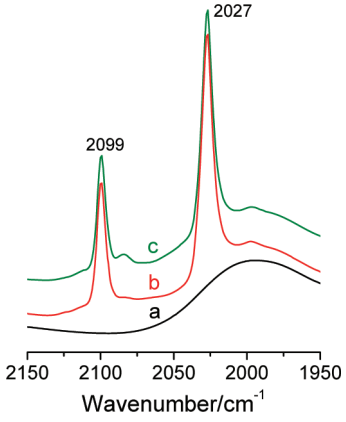

Figure 8. IR spectra (absorbance) in the ν_{CO} stretching region characterizing zeolite-supported $Ir(C_2H_4)_2$ in flowing helium (a); after contact with a pulse of CO (20 mL at 298 K and 1 bar) in flowing helium at 298 K (b); and after treatment in flowing $C_2H_4 + H_2$ at 298 K and 1 bar for 30 min followed by a pulse of CO (20 mL at 298 K and 1 bar) in flowing helium at 298 K (c).

$Ir(CO)_2$ species (Figure S1 in Supporting Information) is consistent with the inference that the sample incorporated mononuclear iridium species and not clusters (ν_{CO} bands characterizing iridium clusters are expected in the region of 1800–1900 cm^{-1}, for edge- and face-bridging CO ligands bonded to neighboring Ir atoms[32−34]).

Reaction of Zeolite-Supported Iridium Dicarbonyl Complexes with C_2H_4 and C_2H_4 + CO. To further probe the reactivity of the iridium complexes, the quite stable supported $Ir(CO)_2$ was treated with flowing ethylene to determine whether it would displace carbonyl ligands. Changes in the IR spectra in the ν_{CO} stretching region occurred rapidly, demonstrating that reaction indeed occurred: the initial ν_{CO} bands at 2027 and 2099 cm^{-1} decreased in intensity with time, and disappeared after 10 min, with the simultaneous growth of two new bands, at 2041 and 2083 cm^{-1} (Figure 9), which are

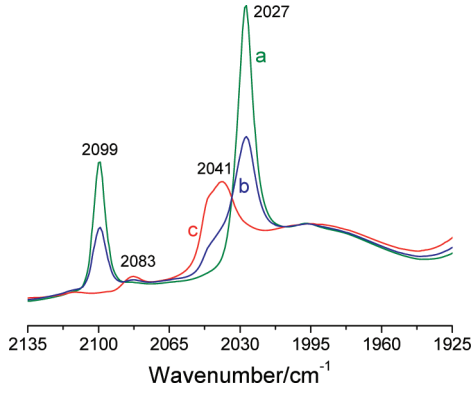

Figure 9. IR spectra (absorbance) in the ν_{CO} stretching region characterizing changes in the sample initially consisting of $Ir(CO)_2$ on HSSZ-53 zeolite as it was present initially (a) and after it had been exposed to flowing C_2H_4 at 298 K for periods of 1 (b) and 10 min (c).

assigned to $Ir(C_2H_4)(CO)$ and $Ir(C_2H_4)_2(CO)$, respectively. The assignment is based on an investigation of the isostructural $Ir(CO)_2$ complex supported on a similar zeolite, dealuminated HY, as it was subjected to the same treatment conditions,[35] whereby the initial ν_{CO} bands at 2038 and 2109 cm^{-1} were shifted to 2054 and 2087 cm^{-1}, respectively (Table 2). In agreement with the assignment, the total area under these two new bands was found to be approximately 50% of the area of the two ν_{CO} bands characterizing the respective $Ir(CO)_2$ species, indicating that each iridium species incorporated only one CO ligand in the HSSZ-53 sample. Furthermore, the IR spectra in the ν_{CH} stretching region characterizing HSSZ-53-supported $Ir(CO)_2$ in a stream of C_2H_4 at 298 K and 1 bar show the appearance of a band at 3092 cm^{-1} (Figure 3d), a clear indication of the formation of ethylene ligands π-bonded to the iridium.

The percentages of $Ir(CO)(C_2H_4)_2$ and $Ir(CO)(C_2H_4)$ species formed from this treatment were approximately 10 and 90, respectively, estimated on the basis of the peak area ratio in the IR spectra.[36] In contrast to this result, the data characterizing the isostructural $Ir(CO)_2$ complex supported on HY zeolite[35] show that a much higher percentage of $Ir(C_2H_4)_2(CO)$, approximately 40, was formed in the identical treatments (Table 2).

Figure 10 shows IR spectra in the ν_{CO} stretching region recorded when the zeolite HSSZ-53-supported iridium dicarbonyl complex was brought in contact with a stream of C_2H_4 + CO (2:1 molar ratio) at 298 K and 1 bar. The ν_{CO} bands at 2027 and 2099 cm^{-1} remained almost unchanged in intensity, indicating that the $Ir(CO)_2$ complex was quite stable when CO was present in the gas phase. This result is contrasted with that observed with the isostructural $Ir(CO)_2$ complex supported on zeolite HY, for which the initial ν_{CO} bands at 2038 and 2109 cm^{-1} characterizing the iridium dicarbonyl quickly shifted to 2087 and 2111 cm^{-1} in the presence of flowing C_2H_4 + CO;[35] these bands were assigned[35] to new species: $Ir(C_2H_4)_2(CO)$ and $Ir(C_2H_4)(CO)_2$, respectively, on the basis of transient IR, EXAFS, and XANES data.

In contrast to the behavior of the zeolite HSSZ-53- and zeolite HY-supported samples, the isostructural $Ir(CO)_2$ complex supported on MgO showed no reactivity with C_2H_4.[35] The results, summarized in Table 2, show clear evidence of the effect of the support—as a ligand—on the reactivity of the isostructural iridium complexes.

dx.doi.org/10.1021/cs300139p | ACS Catal. 2012, 2, 1002–1012

Table 2. Structural Characterization and Catalyst Performance Data Characterizing Samples Initially in the Form of $Ir(C_2H_4)_2$ Complexes on Various Supports (Zeolite HY, Zeolite HSSZ-53, and MgO) under Various Treatment Conditions at 298 K and 1 bar

support	species formed and ν_{CO} peaks after CO pulse (cm^{-1})	species formed in flowing C_2H_4 after CO pulse[a]	species formed in flowing C_2H_4 + CO after CO pulse	stability of ethylene ligand in flowing H_2	ethylene hydrogenation TOF (s^{-1})[b]	H–D exchange in reaction of H_2 + D_2 (% conversion)[c]		refs
						with C_2H_4	without C_2H_4	
zeolite HY	$Ir(CO)_2$ 2038, 2109	60% $Ir(CO)(C_2H_4)_2$, 40% $Ir(CO)(C_2H_4)_2$	70% $Ir(CO)_2(C_2H_4)$, 30% $Ir(CO)(C_2H_4)_2$	rapidly converted to ethyl	0.69	11	100[d]	19, 35
zeolite HSSZ-53	*$Ir(CO)_2$ 2027, 2099*	90% $Ir(CO)(C_2H_4)$, 10% $Ir(CO)(C_2H_4)_2$	100% $Ir(CO)_2$	rapidly converted to ethyl	0.41	50	100[d]	this work
MgO	$Ir(CO)_2$ 1967, 2051	100% $Ir(CO)_2$	100% $Ir(CO)_2$	stable as ethylene	0.03	0.72	44	19, 35

[a]Fractions of each species were estimated on the basis of the area under each peak in the ν_{CO} stretching region relative to the areas of the two ν_{CO} bands characterizing the respective $Ir(CO)_2$ species. [b]Calculated from differential conversions at time on stream = 0 (extrapolated from the corresponding conversion vs time-on-stream curves), assuming that all the Ir atoms were accessible to reactants (Supporting Information Figure S3). [c]Fractional conversion relative to equilibrium in the H–D exchange in the presence of C_2H_4. Reaction conditions: 298 K, 1 bar, 0.2 bar H_2, 0.2 bar D_2, 0.2 bar C_2H_4, and the balance helium. [d]Conversions reached equilibrium value that could not be lowered by either decreasing sample mass or decreasing feed flow rates within the ranges allowed by our apparatus.

Figure 10. IR spectra (absorbance) in the ν_{CO} stretching region characterizing changes in the sample initially consisting of $Ir(CO)_2$ on HSSZ-53 zeolite as it was present initially (a) and after it had been exposed to flowing CO + C_2H_4 at 298 K for 30 min (b).

Catalytic Hydrogenation of Ethylene. The performance of the zeolite HSSZ-53-supported $Ir(C_2H_4)_2$ complex as a catalyst was evaluated in a tubular packed-bed plug-flow reactor at 298 K and 1 bar as it was in contact with flowing H_2 + C_2H_4 (2:1 molar ratio). The data were used to determine the initial rate of the catalytic reaction (measured as the turnover frequency, TOF, the rate per Ir atom), as described previously.[19] The zeolite support alone lacked a measurable catalytic activity under the conditions of the experiment. The catalyst deactivated over time reflecting changes in the ligand environment of the iridium and accumulations of hydrocarbons on the support surface, as evidenced by IR spectroscopy (Supporting Information Figures S2 and S3).

Catalytic Reaction of H_2 with D_2: H–D Exchange. In the H–D exchange experiment, mixtures of H_2, D_2, and C_2H_4 (molar ratio $H_2/D_2/C_2H_4$ = 1:1:1, diluted in helium) flowed through a bed initially containing the zeolite HSSZ-53-supported $Ir(C_2H_4)_2$ complex catalyst at 298 K and 1 bar. The concentration of HD in the product was measured by mass spectrometry, and fractional conversions relative to equilibrium were measured as described previously.[19]

A comparison of catalyst performance data for ethylene hydrogenation and H–D exchange characterizing the supported iridium catalysts initially in the form of $Ir(C_2H_4)_2$ complexes is shown in Table 2. Results are presented for catalysts on each of the following supports under identical reaction conditions: dealuminated HY zeolite (zeolite HY),[19] MgO,[19] and zeolite HSSZ-53.

Spectroscopic Characterization of Working Catalyst for Ethylene Hydrogenation. IR experiments characterizing the working catalyst (initially zeolite HSSZ-53-supported $Ir(C_2H_4)_2$ complex) were conducted under the same conditions stated above for catalytic ethylene hydrogenation (flowing H_2 + C_2H_4, 2:1 molar ratio) with 30 mg of the catalyst sample in an IR cell serving as a flow reactor. The data show changes in the ligand environment of the iridium depending on the reactive gas atmosphere. Contact with this reactant stream led to the rapid disappearance of the bands at 3038 and 3057 cm^{-1}(Figure 3c), characterizing the π-bonded ethylene ligands, and the concomitant growth of bands at 2860, 2874, 2930, and 2960 cm^{-1}, ascribed to ethyl ligands on iridium (Figure S2 in Supporting Information).[37,38] These results are consistent with those characterizing the isostructural $Ir(C_2H_4)_2$ complex supported on dealuminated zeolite HY, but they are contrasted

with those characterizing the isostructural iridium complex supported on MgO, in which the π-bonded ethylene ligands were found to be highly stable even after 2 h of contact with H_2 (Table 2). The results suggest that, once the sample incorporating the zeolite support had been brought in contact with H_2, the initial π-bonded ethylene ligands were rapidly hydrogenated to form ethyl ligands; this point is addressed further in the Discussion section.

Spectroscopic and STEM Characterization of the Used Catalyst. After 30 min on stream during ethylene hydrogenation catalysis in the IR cell, the gas-phase C_2H_4 and H_2 were purged with helium, and a pulse of CO (20 mL) in helium was injected into the cell. The IR spectra show the immediate appearance of the two ν_{CO} bands, at 2027 and 2099 cm^{-1}, characterizing the $Ir(CO)_2$ species—and no evidence of other ν_{CO} bands that would indicate iridium clusters (Figure 8c).[32−34]

Consistent with the IR spectra, HAADF-STEM images of the used catalyst show isolated Ir atoms and no evidence of clusters (Figure 5B). Thus, the spectra and images indicate that no aggregation had occurred, and the mononuclear iridium complexes are inferred to be the true catalyst under our reaction conditions.

DISCUSSION

Formation of Highly Dispersed Mononuclear Iridium Complexes in 1-D Zeolite Channels. Zeolite HSSZ-53 is a highly crystalline material, as indicated by X-ray crystallographic data,[9] with a structure incorporating parallel nonintersecting channels corresponding to crystals with needle-like structures (Figure 6). The zeolite has a Si/Al ratio of 23, and is essentially free of amorphous species which are, for example, created in the dealumination processes of dealuminated Y zeolite.[39,40]

With this structure, when zeolite HSSZ-53 is viewed from the [010] projection (Figure 1), the contrasting overlap of the zeolite framework and the 14-ring channels creates unique alternating bright and dark regions in the images (Figure 5), and these provide a unique opportunity for distinguishing heavy metal atoms in the channels from the zeolite framework elements—and therefore the opportunity to image catalytic sites within the channels. In contrast, attempts to image the 3-dimensional zeolite Y have been limited by its complicated framework structure and by its sensitivity to the electron beam.[41,42]

Taking advantage of the structure of HSSZ-53, we prepared supported iridium complexes that the IR and EXAFS spectra identify and show to be highly uniform. The STEM images of the initially prepared sample demonstrate that these complexes were site-isolated and well separated within the one-dimensional channels, an almost ideal array of individual catalytic sites.[27] The images recorded after prolonged (30-s) exposure to the electron beam give no evidence of aggregation of the iridium without destruction of the zeolite frame (in contrast to the behavior of the isostructural complexes on MgO, which underwent rapid aggregation to form clusters under the influence of the electron beam[26]), thereby demonstrating another advantage of the channel-confined catalytic species: a high degree of site-isolation and stability.

This sample is the first that incorporates well-defined metal complexes anchored in one-dimensional zeolite channels. In contrast, earlier attempts to prepare such samples in the 12-ring zeolites mordenite and HSSZ-42 were stymied by the restricted transport of the precursors $Ir(C_2H_4)_2(acac)$ and $Rh(C_2H_4)_2(acac)$ (with critical diameters of 4 × 6 Å) in the narrow channels (7.0 × 6.5 and 6.4 × 6.4 Å, respectively).[43]

These advantages of the zeolite HSSZ-53-supported iridium complexes allow a precise assessment of their reactivity and catalytic properties, as summarized in the following paragraphs.

Influence of Support on Electronic Properties of Isostructural Iridium Complexes. Differences in reactivities with CO and C_2H_4 were observed for the zeolite HY- and HSSZ-53-supported $Ir(CO)_2$ complexes, and they both were found to be more reactive than the isostructural complex supported on MgO—the carbonyl ligands in this complex were not replaced under our conditions by C_2H_4, either in a pure stream or in a mixture of C_2H_4 with CO (Table 2).[35] We suggest that the different reactivities of the iridium complexes on these supports may be explained by the different electron withdrawing/donating properties of the zeolites.

When a CO ligand is bonded to an electron-deficient metal atom, the C−O bond is strengthened as a result of the increase in electron density transferred from CO to the metal through σ donation, which leads to blue-shifts in the ν_{CO} frequencies; in contrast, when the metal is electron-rich, π back-donation from the metal to CO dominates, which weakens the C−O bond and causes a red-shift of the ν_{CO} bands.[44] In comparison with the ν_{CO} frequencies characterizing the $Ir(CO)_2(acac)$ precursor in tetrahydrofuran solution (2002 and 2082 cm^{-1}),[45] those characterizing the supported $Ir(CO)_2$ complexes on zeolites HY and HSSZ-53 are blue-shifted, whereas those characterizing the MgO-supported $Ir(CO)_2$ are red-shifted (Table 2). These results demonstrate that, as supports, both zeolite HY and HSSZ-53 are electron-withdrawing ligands, whereas MgO is an electron-donating ligand.[46] The data of Table 2 lead to the following qualitative comparison of the electron densities of the iridium in the complexes on the three supports: Ir/HY < Ir/HSSZ-53 ≪ Ir/MgO.

Influence of Support on Reactivity and Catalytic Activity of Iridium Complex. Figure 11 shows the catalytic performance data for ethylene hydrogenation and H−D exchange reactions, plotted as a function of the electron deficiency of the supported $Ir(C_2H_4)_2$ complex as indicated by the ν_{CO} frequencies of the carbonylated species (as explained in the preceding section, the ν_{CO} frequencies of the carbonylated complexes indicate the electron deficiency of the iridium complexes). The data show a strong correlation between the electron density on the iridium and the catalytic performance, with the rate of ethylene hydrogenation increasing almost linearly with the ν_{CO} frequencies of the carbonylated complexes, as the Ir atom becomes more electron deficient. Although the catalytic activity for H−D exchange (measured by the conversion) increased dramatically when the support was switched from the electron-donating MgO to the electron-withdrawing zeolite (Table 2 and Figure 11), it did not follow the same linear trend as shown for the ethylene hydrogenation activity (measured by reaction rate). We suggest that these observations may indicate the differences in the abilities of the iridium complexes to activate H_2 and C_2H_4, as discussed in the following sections.

Our recent investigation demonstrated,[19] on the basis of time-resolved IR and EXAFS data, that the rate of ethylene hydrogenation catalyzed by the supported iridium ethylene complex is controlled by its ability to simultaneously activate both reactants, H_2 and ethylene. Our data, in agreement with the previous results, provide further evidence of how the supports affect the reactivity of the iridium complex with H_2

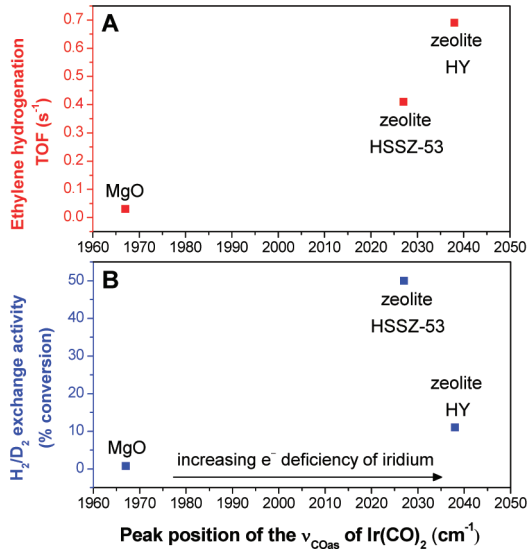

Figure 11. Correlation between rate of catalytic ethylene hydrogenation (A) and H_2/D_2 exchange activity in the presence of C_2H_4 (B) of the supported iridium complex on various supports and the frequency of ν_{CO} bands when the iridium complex had been carbonylated by treatment with a pulse of CO (20 mL) in helium at 298 K (a higher ν_{CO} frequency indicates that the iridium complex is more electron deficient).

and C_2H_4. The data show the following: (a) when in contact with H_2, the π-bonded ethylene ligands are facilely converted to ethyl when the support is zeolite HSSZ-53, whereas they are stable as ethylene when the support is MgO; (b) the H−D exchange reaction catalyzed by zeolite HSSZ-53-supported iridium complexes is much faster than that catalyzed by the MgO-supported complexes; and (c) the catalytic activity for ethylene hydrogenation when the support is zeolite HSSZ-53 is an order of magnitude higher than when the support is MgO. These observations are consistent with the inference[19] that the reaction rate can be significantly increased as a result of increasing the H_2 activation rate, when the support is switched from the electron-donating MgO to the electron-withdrawing zeolite.[19] However, there had been a lack of evidence to fully elucidate the rate limiting step when H_2 activation is no longer rate limiting (when iridium is electron deficient). The data presented here provide basis for such an elucidation, as discussed below.

In the absence of C_2H_4, the activities for H−D exchange catalyzed by the isostructural $Ir(C_2H_4)_2$ complexes on zeolite HY and on HSSZ-53 are extremely high (Table 2), with the conversions reaching the equilibrium value that could not be lowered by either decreasing the catalyst sample mass or decreasing the reactant flow rate within the ranges allowed by our apparatus. However, when C_2H_4 was cofed with $H_2 + D_2$ (with ethylene hydrogenation occurring), the H_2 dissociation was faster whereas the rate of ethylene hydrogenation was lower for the zeolite HSSZ-53-supported iridium complex than for the zeolite HY-supported complex. This comparison is explained by the differences in the competitive adsorption of the two reactants. As shown by the IR data (Table 2) characterizing the carbonylated iridium complex in flowing C_2H_4, the interaction between the iridium and gas-phase C_2H_4 is weaker when the support is zeolite HSSZ-53 than when it is zeolite HY (only approximately 10% of the complexes were in the form of $Ir(CO)(C_2H_4)_2$ when the support was zeolite HSSZ-53, whereas approximately 40% was in this form when the support was zeolite HY).

The inference that the competitive adsorption of the two reactants influences the rate-limiting step is supported by the mass spectra characterizing the effluent gas flowing from the reactor when the catalyst was in contact with a stream of $C_2H_4 + D_2$ (under conditions of ethylene deuteration), showing that the major product of the reaction was $C_2H_4D_2$, with only negligible formation of $C_2H_3D_3$ and $C_2H_2D_4$ (Figure S5). This result points to a migratory insertion as the likely rate-determining step, with the simultaneous adsorption of C_2H_4 and activation of D_2 (or H_2) playing a role in the catalysis.[47] The weaker affinity of the iridium complex on zeolite HSSZ-53 for ethylene ligands accounts for the higher activity for H_2 dissociation when both reactants compete for bonding positions on the same catalytic sites. Thus, the observation that the rate of ethylene hydrogenation catalyzed by the zeolite HSSZ-53-supported iridium complex is lower than that catalyzed by the zeolite HY-supported complex, together with the inference that the zeolite HSSZ-53-supported iridium complex interacts more weakly with C_2H_4, suggests that the rate of the reaction catalyzed by the electron-deficient iridium complexes (on zeolite supports) is limited by adsorption of C_2H_4, not by H_2 activation.

In summary, the results presented here, together with results reported previously, indicate that the rate of ethylene hydrogenation catalyzed by the isostructural $Ir(C_2H_4)_2$ complexes is limited by the H_2 dissociation when the iridium is electron rich (on the MgO support), whereas the rate-limiting step is C_2H_4 adsorption when the iridium is electron deficient (on the zeolite supports).

CONCLUSIONS

The molecular iridium complex catalyst supported on the highly crystalline zeolite HSSZ-53 is the first example of a well-defined metal complex anchored in one-dimensional zeolite channels. This highly uniform supported molecular catalyst is ideally suited for elucidation of its chemistry. The data presented here, together with results characterizing isostructural $Ir(C_2H_4)_2$ complexes on HY zeolite and on MgO, show the influence of the supports as ligands controlling the electronic properties of the iridium complexes and influencing their reactivities with gas-phase CO, C_2H_4, and H_2 as well as their catalytic activities for ethylene hydrogenation and H−D exchange in the reaction of $H_2 + D_2$. The results identify the rate-limiting steps in ethylene hydrogenation catalysis: H_2 activation on the electron-donating MgO and C_2H_4 adsorption on the electron-withdrawing zeolites.

EXPERIMENTAL METHODS

Materials and Sample Preparation. Standard methods were used for sample synthesis and handling with the exclusion of moisture and air. H_2 was supplied by Airgas (99.999%) and purified by passage through traps containing reduced Cu/Al_2O_3 and activated zeolite 4A to remove traces of O_2 and moisture, respectively. Helium (Airgas, 99.999%) and ethylene (Airgas, 99.99%) were purified by passage through similar traps. CO (Matheson, 99.999%), in a 10% mixture in helium, was purified by passage through a trap containing activated γ-Al_2O_3 particles and zeolite 4A to remove any traces of metal carbonyls from the high-pressure gas cylinders and moisture, respectively. Deuterium (99.8% D_2) was purchased from Cambridge Isotope

dx.doi.org/10.1021/cs300139p | ACS Catal. 2012, 2, 1002−1012

Laboratories. The aluminosilicate HSSZ-53 zeolite, synthesized as described elsewhere,[9] was calcined in flowing, dry O_2 as its temperature was increased at a constant rate from room temperature to 723 K over 5 h followed by a soak at 723 K for an additional 1 h, after which the O_2 flow to the reactor was stopped and the reactor evacuated at 723 K for an additional 1 h. After calcination, the zeolite was isolated and stored in an argon-filled glovebox (MBraun, with H_2O concentrations <0.5 ppm and O_2 concentrations <5 ppm) until it was used. *n*-Pentane solvent (Fisher, 99%) was dried and purified by column chromatography (Grubbs apparatus, MBraun SPS) in the presence of argon.

The precursor $Ir(C_2H_4)_2(C_5H_7O_2)$ was synthesized as described elsewhere.[16] To prepare the zeolite-supported iridium complex, $Ir(C_2H_4)_2(C_5H_7O_2)$ and the calcined zeolite powder in a Schlenk flask were slurried in dried *n*-pentane that was initially at ice temperature. The stirred slurry was warmed to room temperature, and, after 1 day, the solvent was removed by evacuation for 1 day, so that all the iridium remained in the zeolite. The resultant solid, containing 1.0 wt % iridium, was stored in the argon-filled glovebox.

IR Spectroscopy and Mass Spectrometry. A Bruker IFS 66v/S spectrometer with a spectral resolution of 2 cm^{-1} was used to collect transmission IR spectra of powder samples. Approximately 30 mg of solid sample in the glovebox was pressed into a thin wafer and loaded into a cell that served as a flow reactor (In-situ Research Institute, Inc., South Bend, IN). The cell was sealed and connected to a flow system that allowed recording of spectra while the reactant gases flowed through the cell at reaction temperature. Each spectrum is the average of 64 scans.

The effluent gas was analyzed by mass spectrometry (Balzers OmniStar).

Ethylene Hydrogenation Catalysis in a Flow Reactor. Ethylene hydrogenation catalysis was carried out in a conventional laboratory once-through tubular plug-flow reactor that was nearly isothermal. The catalyst powder (30 mg), diluted with 10 g of inert, nonporous α-Al_2O_3, was loaded into the reactor in a glovebox and transferred to the flow system without exposure to air. In the catalytic reaction experiments, the feed C_2H_4 partial pressure was 200 mbar and the feed H_2 partial pressure was 400 mbar, with the balance being helium. The feed flow rate was 100 mL/min and the pressure was atmospheric. The temperature was 298 ± 1 K.

Products were analyzed by online gas chromatography with an HP-6890 gas chromatograph equipped with a 50 m × 0.53 mm DB-624 capillary column (J & W Scientific) and a flame ionization detector. The effluent gas from the reactor was sampled every 12 min for analysis. The ethylene conversions were less than 5%, and the reactor was approximated as differential.

H−D Exchange Experiments. Measurements were carried out in a plug-flow reactor the same as that used for ethylene hydrogenation. The catalyst (30 mg), mixed with 5 g of particles of inert, nonporous α-Al_2O_3, was loaded into the reactor in a glovebox and transferred to the flow system without exposure to air. The feed C_2H_4, H_2, and D_2 partial pressures were each 200 mbar, and the balance was helium. The total flow rate was 100 mL/min. The pressure was atmospheric and the temperature 298 ± 1 K. Mass spectra of the gases introduced into the flow system and of the effluent stream flowing from the reactor were measured with an online Balzers OmniStar mass spectrometer running in multi-ion monitoring mode. Specifically, changes in the signal intensities of H_2 (m/z = 2), D_2 (m/z = 4), HD (m/z = 3), CO (m/z = 28), C_2H_4 (m/z = 26, 27, and 28), C_2H_6 (m/z = 26, 27, 28, and 30), C_4H_8 (m/z = 41 and 55), C_4H_{10} (m/z = 43 and 56), $C_2H_4D_2$ (m/z = 32), $C_2H_3D_3$ (m/z = 33) and $C_2H_2D_4$ (m/z = 34) were recorded. The reported intensity values were corrected by subtracting background intensities recorded while the reaction mixture bypassed the flow reactor.

X-ray Absorption Spectroscopy. Ir L_{III}-edge X-ray absorption spectra were recorded at beamline X18-B at the National Synchrotron Light Source (NSLS) at Brookhaven National Laboratory. The storage ring electron energy and ring currents were 2.8 GeV and 200−300 mA, respectively. A Si (111) double-crystal monochromator was used, which was detuned to 80% of maximum intensity to reduce the interference of higher harmonics present in the X-ray beam.

In an N_2-filled glovebox at NSLS, the powder catalyst sample was pressed into a wafer, mounted in a cell,[48] and maintained under vacuum (10^{-5} kPa) at liquid nitrogen temperature during the data collection. The mass of each sample (approximately 0.3 g) was chosen for optimal absorption measurements at the Ir L_{III} edge (11215 eV), giving an X-ray absorbance of approximately 2.0 calculated at an energy 50 eV greater than the absorption edge. Spectra were collected in transmission mode by use of ion chambers mounted on each end of the sample cell. For calibration purposes, measurement of the absorption of a platinum foil, placed after the sample, was carried out simultaneously.

EXAFS Data Analysis. The X-ray absorption edge energy was calibrated with the measured signal at the Pt L_{III} edge of the platinum foil that was scanned simultaneously with the sample; the edge was taken to be the inflection point at 11564 eV. The data were normalized by dividing the absorption intensity by the height of the absorption edge.

The EXAFS data were analyzed with the software ATHENA of the IFEFFIT[49,50] package and the software XDAP, developed by Vaarkamp et al.[51] Each spectrum subjected to analysis was the average of two to four consecutively recorded spectra. ATHENA was used for edge calibration, deglitching, and data normalization. XDAP was used for background removal, normalization, and conversion of the data into an EXAFS (χ) file. A "difference-file" technique[52] involving analysis of individual shells was applied with XDAP for determination of optimized fit parameters. Each spectrum was processed by fitting a second-order polynomial to the pre-edge region and subtracting this from the entire spectrum. The functional that was minimized and the function used to model the data are stated elsewhere.[52] The background was subtracted by using cubic spline routines. Reference backscattering phase shifts were calculated with the software FEFF7[53] from crystallographic data. $Ir(C_2H_4)_2(C_5H_7O_2)$[16] was used as a standard for Ir−O, Ir−C, and Ir−C_{long} contributions; Ir−Al alloy[54] was used as a standard for Ir−Al contributions, and iridium metal[54] was used for Ir−Ir contributions. These contributions were selected as candidates for the EXAFS analyses because they were all considered plausible on the basis of reports of similar supported organometallic complexes and clusters.[18] Iterative fitting was done in *R* (distance) space with the Fourier-transformed EXAFS (χ) data until optimum agreement was attained between the calculated k^1- and k^3-weighted EXAFS data and each candidate model.

The error in the data was calculated as the root-mean-square of the value obtained by subtraction of smoothed χ data from

the background-subtracted experimental χ values. Goodness of fit values were calculated with the software XDAP, as follows:

$$\text{goodness of fit} = \frac{\nu}{\text{NPTS}(\nu - N_{\text{free}})} \sum_{i=1}^{\text{NPTS}} \left(\frac{\chi_{\text{exp},i} - \chi_{\text{model},i}}{\sigma_{\text{exp},i}} \right)^2 \quad (1)$$

Here the terms χ_{model} and χ_{exp} are the model and experimental EXAFS values, respectively; σ_{exp} is the error in the experimental results; ν is the number of independent data points in the fit range; NPTS is the actual number of data points in the fit range; and N_{free} is the number of free parameters. The number of parameters used in the fitting was always less than the statistically justified number, computed according to the Nyquist theorem:[55] $n = (2\Delta k \Delta r/\pi) + 1$, where Δk and Δr, respectively, are the k (wave vector) and r (interatomic distance) ranges used in the fitting.

Aberration-Corrected STEM Imaging. Images were obtained with a JEOL JEM-2100F electron microscope at the University of California, Davis. The microscope was equipped with a FEG, operating at 200 kV, with a CEOS hexapole probe (STEM) aberration corrector. The images were captured by a HAADF detector with a collection semiangle of 75−200 mrad and a probe convergence semiangle of 17.1 mrad. The imaging dose was approximately 10^5 e^- $Å^{-2}$. Prior to imaging of the sample, the aberration corrector was aligned with a Pt/Ir on holey carbon standard sample (SPI supplies) until atomic resolution of the metal particles was achieved and the lattice spacing of the metals in the standard sample were confirmed.

Sample Handling for Electron Microscopy. To minimize the exposure to air and moisture, powder samples in the argon-filled glovebox were loaded onto a lacey carbon film, 300-mesh copper grid (Ted-Pella). The grid was placed into an Eppendorf tube that was sealed with Parafilm. Still in the glovebox, each Eppendorf tube was placed into a stainless-steel Swagelok tube sealed with O-rings for transfer to the microscope. There, an argon-filled glovebag (Glas-Col) was purged five times with ultrahigh-purity argon (Praxair, grade 5.0), and the TEM grid was loaded onto the TEM holder under a blanket of flowing argon in the glovebag. The TEM holder was then inserted into the nearby microscope under a flow of argon, with any exposure to air lasting less than 5 s.

■ ASSOCIATED CONTENT

Supporting Information

Additional IR and EXAFS spectra, details of EXAFS analysis, and catalytic reaction data are included. This material is available free of charge via the Internet at http://pubs.acs.org.

■ AUTHOR INFORMATION

Corresponding Author

*E-mail: bcgates@ucdavis.edu.

Present Address

[‖]Fundamental and Computational Sciences Division, Pacific Northwest National Laboratory, 902 Battelle Boulevard, Richland, WA 99352, USA.

Notes

The authors declare no competing financial interest.

■ ACKNOWLEDGMENTS

We thank Saleh Elomari for providing the organic structure directing agent for the zeolite synthesis and Stacey Zones for helpful comments. This work was supported by the Department of Energy (DOE) Grant FG02-87ER15600 (J.L.) and Grant DE-FG02-03ER46057 (C.A.), and the University of California Lab Fee Program. We acknowledge beam time and the support of the DOE Division of Materials Sciences for its role in the operation and development of beamline X-18B at the National Synchrotron Light Source.

■ REFERENCES

(1) Climent, J.; Corma, A.; Iborra, S. *Chem. Rev.* **2011**, *111*, 1072−1133.
(2) Corma, A. *Catal. Rev. Sci. Eng.* **2004**, *46*, 369−417.
(3) Guzman, J.; Gates, B. C. *Dalton Trans.* **2003**, *17*, 3303−3318.
(4) Tauster, S. J.; Fung, S. C.; Baker, R. T. K.; Horsley, J. A. *Science* **1981**, *211*, 1121−1125.
(5) Stair, P. C. *Nat. Chem.* **2011**, *3*, 345−346.
(6) Davis, M. E. *Nature* **2002**, *417*, 813−821.
(7) Corma, A . *Top. Catal.* **1997**, *4*, 249−260.
(8) Sachtler, W. M. H.; Zhang, Z. *Adv. Catal.* **1993**, *39*, 129−220.
(9) Burton, A.; Elomari, S.; Chen, C. Y.; Medrud, R. C.; Chan, I. Y.; Bull, L. M.; Kibby, C.; Harris, T. V.; Zones, S. I.; Vittoratos, E. S. *Chem.—Eur. J.* **2003**, *9*, 5737−5748.
(10) Breck, D. W. *Zeolite Molecular Sieves: Structure, Chemistry, and Use*; Wiley: New York, 1973.
(11) Van Der Voort, P.; Mathieu, M.; Vansant, E. F.; Rao, S. N. R.; White, M. G. *J. Porous Mater.* **1998**, *5*, 305−316.
(12) Van Der Voort, P.; van Welzenis, R.; de Ridder, M.; Brongersma, H. H.; Baltes, M.; Mathieu, M.; van de Ven, P. C.; Vansant, E. F. *Langmuir* **2002**, *18*, 4420−4425.
(13) Argo, A. M.; Odzak, J. F.; Lai, F. S.; Gates, B. C. *Nature* **2002**, *415*, 623−626.
(14) Argo, A. M.; Odzak, J. F.; Gates, B. C. *J. Am. Chem. Soc.* **2003**, *125*, 7107−7115.
(15) Bent, B. E.; Mate, C. M.; Kao, C.-T.; Slavin, A. J.; Somorjai, G. A. *J. Phys. Chem.* **1988**, *92*, 4720−4726.
(16) Bhirud, V. A.; Uzun, A.; Kletnieks, P. W.; Craciun, R.; Haw, J. F.; Dixon, D. A.; Olmstead, M. M.; Gates, B. C. *J. Organomet. Chem.* **2007**, *692*, 2107−2113.
(17) van't Blik, H. F. J.; van Zon, J. B. A. D.; Huzinga, T.; Vis, J. C.; Koningsberger, D. C.; Prins, R. *J. Am. Chem. Soc.* **1985**, *107*, 3139−3147.
(18) Fierro-Gonzalez, J. C.; Kuba, S.; Hao, Y.; Gates, B. C. *J. Phys. Chem. B* **2006**, *110*, 13326−13351.
(19) Lu, J.; Serna, P.; Aydin, C.; Browning, N. D.; Gates, B. C. *J. Am. Chem. Soc.* **2011**, *133*, 16186−16195.
(20) Uzun, A.; Bhirud, V. A.; Kletnieks, P. W.; Haw, J. F.; Gates, B. C. *J. Phys. Chem. C* **2007**, *111*, 15064−15073.
(21) Ogino, I.; Gates, B. C. *J. Am. Chem. Soc.* **2008**, *130*, 13338−13346.
(22) Liang, A. J.; Bhirud, V. A.; Ehresmann, J. O.; Kletnieks, P. W.; Haw, J. F.; Gates, B. C. *J. Phys. Chem. B* **2005**, *109*, 24236−24243.
(23) Pennycook, S. J.; Jesson, D. E. *Ultramicroscopy* **1991**, *37*, 14−38.
(24) Hirsch, E. H. *Nature* **1981**, *293*, 759.
(25) Bursill, L. A.; Thomas, J. M.; Rao, K. J. *Nature* **1981**, *289*, 157−158.
(26) Uzun, A.; Ortalan, V.; Hao, Y.; Browning, N. D.; Gates, B. C. *ACS Nano* **2009**, *3*, 3691−3695.
(27) Aydin, C.; Lu, J.; Liang, A. J.; Chen, C.-Y.; Browning, N. D.; Gates, B. C. *Nano Lett.* **2011**, *11*, 5537−5541.
(28) Burkhardt, I.; Gutschick, D.; Landsmesser, H.; Miessner, H. In *Zeolite Chemistry and Catalysis*; Jacobs, P. A., Ed.; Elsevier: Amsterdam, 1991; pp 215−222.
(29) Solymosi, F.; Novak, E.; Molnar, A. *J. Phys. Chem.* **1990**, *94*, 7250−7255.

(30) Mihaylov, M.; Ivanova, E.; Thibault-Starzyk, F.; Daturi, M.; Dimitrov, L.; Hadjiivanov, K. I. *J. Phys. Chem. B* **2006**, *110*, 10383−10389.
(31) Miessner, H.; Burkhardt, I.; Gutschick, D.; Zecchina, A.; Morterra, C.; Spoto, G. *J. Chem. Soc., Faraday Trans.* **1989**, *85*, 2113−2126.
(32) Uzun, A.; Gates, B. C. *J. Am. Chem. Soc.* **2009**, *131*, 15887−15894.
(33) Li, F.; Gates, B. C. *J. Phys. Chem. B* **2004**, *108*, 11259−11264.
(34) Hanlan, L. A.; Ozin, G. A. *J. Am. Chem. Soc.* **1974**, *96*, 6324−6329.
(35) Lu, J.; Serna, P.; Gates, B. C. *ACS Catal.* **2011**, *1*, 1549−1561.
(36) For example, the fraction of the iridium present as $Ir(C_2H_4)_2(CO) \cong$ (area of ν = 2083 cm^{-1} band)/(area of ν = 2083 cm^{-1} band + area of ν = 2041 cm^{-1} band).
(37) Morrow, B. A. *Can. J. Chem.* **1970**, *48*, 2192−2196.
(38) Newell, H. E.; McCoustra, M. R. S.; Chesters, M. A.; De La Cruz, C. *J. Chem. Soc., Faraday Trans.* **1998**, *94*, 3695−3698.
(39) Janssen, A. H.; Koster, A. J.; de Jong, K. P. *Angew. Chem., Int. Ed.* **2001**, *40*, 1102−1104.
(40) Van Donk, S.; Janssen, A. H.; Bitter, J. H.; de Jong, K. P. *Catal. Rev.* **2003**, *45*, 297−319.
(41) Pan, M.; Crozier, P. A. *Ultramicroscopy* **1993**, *48*, 332−340.
(42) Ortalan, V.; Uzun, A.; Gates, B. C.; Browning, N. D. *Nat. Nanotechnol.* **2010**, *5*, 506−510.
(43) Ogino, I.; Chen, C.-Y.; Gates, B. C. *Dalton Trans.* **2010**, *39*, 8423−8431.
(44) Hadjiivanov, K. I.; Vayssilov, G. N. *Adv. Catal.* **2002**, *47*, 308−511.
(45) Bonati, F.; Ugo, R. *J. Org. Chem.* **1968**, *11*, 341−352.
(46) Cotton, F. A.; Wilkinson, G. *Advanced Inorganic Chemistry*; Wiley-Interscience, New York, 1967.
(47) Collman, J. P.; Hegedus, L. S.; Norton, J. R.; Finke, R. G. *Principles and Applications of Organotransition Metal Chemistry*, 2nd ed.; University Science Books: Mill Valley, CA, 1987.
(48) Jentoft, R. E.; Deutsch, S. E.; Gates, B. C. *Rev. Sci. Instrum.* **1996**, *67*, 2111−2112.
(49) Newville, M.; Ravel, B.; Haskel, D.; Rehr, J. J.; Stern, E. A.; Yacoby, Y. *Phys. B* **1995**, *208/209*, 154−156.
(50) Newville, M. *J. Synchrotron Rad.* **2001**, *8*, 96−100.
(51) Vaarkamp, M.; Linders, J. C.; Koningsberger, D. C. *Phys. B* **1995**, *209*, 159−160.
(52) Koningsberger, D. C.; Mojet, B. L.; van Dorssen, G. E.; Ramaker, D. E. *Top. Catal.* **2000**, *10*, 143−155.
(53) Zabinsky, S. E.; Rehr, J. J.; Ankudinov, A.; Albers, R. C.; Eller, M. J. *Phys. Rev. B.* **1995**, *52*, 2995−3009.
(54) Pearson, W. B.; Calvert, L. D.; Villars, P. *Pearson's Handbook of Crystallographic Data for Intermetallic Phases*; American Society for Metals: Metals Park, OH, 1985.
(55) Lytle, F. W.; Sayers, D. E.; Stern, E. A. *Phys. B* **1989**, *158*, 701−722.